GSA DATA REPOSITORY 2014078

Supplemental Material for

Presence of an intra-lithospheric discontinuity in the central and western North China Craton: implications for destruction of the craton

Ling Chen, Mingming Jiang, Jinhui Yang, Zigen Wei, Chuanzhou Liu, Yuan Ling

State Key Laboratory of Lithospheric Evolution, Institute of Geology and Geophysics, Chinese Academy of Sciences, Beijing 100029, China

Data and Imaging Method

Teleseismic waveform data used in this study came from a linear seismic array deployed by the Institute of Geology and Geophysics, Chinese Academy of Sciences under the “Destruction of the North China Craton (DNCC)” project, a multidisciplinary scientific project launched by the NSF of China in 2008. The seismic array ran roughly E-W from around the boundary between the eastern NCC and the TNCO, crossed the Ordos block and ended at the Qilian orogenic belt which borders the NCC to the southwest (Fig. 1), with a total length of ~1000 km. It consists of 64 broadband stations with an average intra-station distance of ~15 km. Each station operated for a period of 10-18 months from December 2006 to May 2008.

In this study we investigated the lithospheric structure of the central and western NCC using the S and P receiver function (RF) data from this array. S and P RFs contain information of S to P (Sp) and P to S (Ps) conversions, respectively, from deep velocity discontinuities. P RF imaging has proven to be efficient in recovering complex structural features of the Moho and deep mantle discontinuities such as those in the mantle transition zone (e.g., Zhu and Kanamori, 2000; Ai et al., 2007; Nábelek et al., 2009). However, it is difficult to produce a clear shallow upper-mantle image in many cases due to the significant interference of the crustal multiples with the Ps signals (e.g., Wittlinger and Farra, 2007; Chen, 2009). In contrast to P RFs, S RFs are free from inferences of crustal multiples and have been widely used to detect discontinuities in the shallow upper mantle, especially the LAB at local to regional scales (e.g., Li et al., 2004; Savage and Silver, 2008; Ford et al., 2010). Recent studies further suggest that a combination of S and P RF imaging can provide more compelling constraints on the lithospheric structure than individual imaging results

(e.g., Rychert et al., 2007; Chen, 2009).

We constructed the S and P RFs for the 64 stations in the same way as we did previously (Chen et al., 2006; 2008; 2009; Chen, 2009). Teleseismic data from 193 events with epicentral distances 55°-85° (Fig. DR1a) and from 536 events with epicentral distances 28°-92° (Fig. DR1d) were selected respectively, resulting in a total of 1250 S RFs and 10700 P RFs with high signal-to-noise ratios for lithospheric structural imaging. The polarity and the time axis of the S RFs were reversed to make them directly comparable with the P RFs. Arrival times of both Sp conversion phases relative to the direct S waves and Ps phases relative to the direct P waves, and the corresponding piercing points of the conversion at depth, were calculated using the average 1-D velocity model for eastern China as we did previously. All the S and P RFs were also moveout-corrected to the case of vertical incidence (horizontal slowness $p = 0$) as required for wave equation-based depth migration (Chen et al., 2005; 2008). We then applied the 2-D wave equation-based poststack migration method for Sp (Chen et al., 2008) and Ps phases (Chen et al., 2005) to the resultant S and P RFs, respectively, to image the lithospheric structure along profile A-A'. The migration for both phases consists of two basic procedures: common conversion point (CCP) stacking and backward wavefield extrapolation (Chen et al., 2005; 2008). The minimum S RF number in each bin in CCP stacking was set to be 50 for effective noise suppression. To make the migrated P and S RF images have compatible lateral resolutions, much larger numbers (> 300) but similar bin sizes were adopted for CCP stacking of P RFs. Figs. DR1b and DR1e give the numbers of S and P RFs in the bins (blue traces) and bin widths (red traces) used in the CCP stacking at 100 and 200 km depths, and Figs. DR1c and DR1f show the corresponding stacked sections of S and P RFs with frequencies 0.03 – 0.5 Hz. Besides the coherent Moho phases at ~5 s, the most pronounced common feature in the two stacked sections is the dominance of strong negative signals in the time range of ~8-12 s. To convert the time-domain stacked sections to depth images, backward wavefield extrapolation was then conducted using a frequency-space domain phase screen propagator (Chen et al., 2005). During this second step of migration, the same 1-D velocity model used in calculation of delay times and piercing point locations was adopted and different ranges of frequency contents of data were superposed to construct the images (Figs. 2, DR2-DR6).

Evaluation on the Reliability of the Lithospheric Image

Both S and P RF images would be affected by many factors, such as, the spatial data coverage, frequency contents of the data, noise, and lateral seismic

heterogeneities. We evaluated the robustness of the lithospheric structural image, especially the intra-lithospheric discontinuity (ILD) and lithosphere-asthenosphere boundary (LAB) identified beneath the Ordos block and TNCO, by frequency analysis and detailed comparisons between the S and P RF migrated images, data images and synthetic modeling results based on the actual data coverage, as well as between results of RF imaging and previous surface wave studies (Figs. DR2-DR7).

We calculated the synthetic seismograms by a 2-D hybrid method (Wen and Helmberger, 1998; Chen et al., 2005) that naturally takes into account the effect of lateral heterogeneities on the waveforms. Given that the dominant periods of our S and P RFs peak at ~4 s and 1s, respectively, we adopted 4 s and 1 s individually in the calculation of these two types of data. We constructed the synthetic S and P RFs, picked them according to the coverage and density of the real data, and performed wave equation poststack migration to construct the corresponding migrated images in the same way as for the real data. The depths of the Moho and the LAB in the synthetic models were designed to resemble those of the imaged real structure. The sharpness of the two discontinuities was set to be uniform over the whole transverse range. We considered a first order Moho discontinuity with the same impedance contrasts as the IASPI91 global model and a 20-km gradient zone with a velocity drop of 4% for the LAB in the synthetic modeling. In some cases, an ILD with a 4% velocity drop over a 10-km depth range at depths similar to the ILD identified in the data images was also incorporated into the synthetic models. The corresponding synthetic images were compared with those without the ILD and the data images to investigate the effects of the ILD to the migrated images, especially of the LAB (e.g., Fig. DR3).

Our ILD and LAB images appear robust based on the results of frequency analysis and images comparisons: 1) The numbers of the S RFs (mostly ≥ 50) and P RFs (mostly ≥ 300) were sufficiently large in each CCP stacking bin, which allow for good noise suppression and signal enhancement; 2) The Sp signals of both discontinuities were consistently imaged using different frequencies of the data (Fig. DR2, except for the image with frequencies lower than 0.2 Hz in which the side lobe of the Moho Sp conversion phase significantly interferes with the Sp phase of the ILD, making it an ambiguous feature); 3) The features of the S and P RF images were consistent with each other and agreed with synthetic modeling results (Figs. DR3–DR5); 4) The nature of the ILD Ps signal was further verified by the close resemblance of its image feature to a true Ps phase but large differences from a crustal multiples when different incident directions of data were considered in imaging (Fig. DR6); and 5) The depth distributions of the ILD and/or the LAB agree broadly with

previous seismic observations on the lithospheric structure of the study region from both 2-D surface wave tomography along the same seismic array (Fig. 2E; Wei, Z.G. et al., unpublished result) and other surface wave studies of various scales (Fig. DR7, Jiang et al., 2013; Huang et al., 2009; Bao et al., 2011) as well as body wave tomography (e.g., Li and vander Hilst, 2010; Zhao et al., 2012).

We estimated the depths of the ILD and the LAB mainly from the highest-frequency S RF image (Fig. 2B, Fig. DR2d) because of it relatively high resolution and little influence from crustal multiples compared to the P RF images. For the ILD, the P RF image of same frequency contents (Fig. 2D) was also considered, since the Ps phase of the ILD is identified without obvious interference from crustal multiples. We mainly considered the portions of the profiles where the numbers of the S RFs are sufficient (50 and above) in the individual CCP stacking bins. To investigate the uncertainties in the depths of the two discontinuities, we adopted different velocity models in imaging, including that incorporating the lateral variations in the crustal and uppermost mantle structure along the profile (e.g., Zhu and Zheng, 2009; Wei et al., 2011; Jiang et al., 2013). The images thus obtained are very similar to those presented here (Figs. 2B, Fig. DR2). We found that the depth uncertainties of the imaged ILD and LAB due to different velocity models adopted in migration are mostly 3~8 km and 5~15 km, respectively, which are comparable to what can be resolved with the real S RF data (~10 km). These values are analogues to the results of our previous studies (Chen et al., 2008; 2009; Chen, 2009) and also to those estimated by other authors for shallow upper mantle discontinuities (e.g., Li et al., 2007; Rychert and Shearer, 2009; Ford et al., 2010; Lekic et al., 2011).

References

Ai Y., Chen Q., Zeng F., Hong X., Ye W., 2007. The crust and upper mantle structure beneath southeastern China. Earth Planet. Sci. Lett. 260, 549-563.

Bao, X., Xu, M., Wang, L., Mi, N., Yu, D., Li, H., 2011. Lithospheric structure of the Ordos Block and its boundary areas inferred from Rayleigh wave dispersion. Tectonophysics, 499, 132-141.

Chen, L., 2009. Lithospheric Structure variations between the eastern and central North China Craton from S- and P-Receiver Function Migration. Phys. Earth Planet. Inter. 173, 216-227.

Chen, L., Cheng C., Wei, Z., 2009. Seismic evidence for significant lateral variations in lithospheric thickness beneath the central and western North China Craton. Earth Planet. Sci. Lett. 286, 171-183.

Chen, L., Wang, T., Zhao, L., and Zheng, T.Y., 2008. Distinct Lateral Variation of Lithospheric thickness in the Northeastern North China Craton. Earth Planet. Sci.

Lett. 267, 56-68.

Chen, L., Wen, L., and Zheng, T., 2005. A Wave Equation Migration Method for Receiver Function Imaging, (I) Theory. J. Geophys. Res. 110, B11309, doi:10.1029/2005JB003665.

Chen, L., Zheng, T.Y., and Xu, W.W., 2006. A thinned lithospheric image of the Tanlu Fault Zone, eastern China: Constructed from wave equation based receiver function migration. J. Geophys. Res. 111, B09312, doi:10.1029/2005JB003974.

Ford, H.A., Fischer, K.M., Abt, D.L., Rychert, C.A., Elkins-Tanton, L.T., 2010. The lithosphere–asthenosphere boundary and cratonic lithospheric layering beneath Australia from Sp wave imaging. Earth Planet. Sci. Lett. 300, 299-310.

Huang, Z., Li, H., and Zheng, Y., 2009. The lithosphere of North China Craton from surface wave tomography. Earth Planet. Sci. Lett. 288, 164–173.

Jiang, M.M., Ai, Y.S., Chen, L., Yang, Y., 2013. Local modification of the lithosphere beneath the central and western North China Craton: 3D constraints from Rayleigh wave tomography. Gondwana Research, http://dx.doi.org/10.1016/j.gr.2012.06.018.

Lekic, V., French, S.W., Fischer, K., 2011. Lithospheric thinning beneath rifted regions of Southern California. Science 334, 783-787.

Li, C., and van der Hilst, R.D., 2010. Structure of the upper mantle and transition zone beneath Southeast Asia from traveltime tomography, J. Geophys. Res. 115, B07308, doi:10.1029/2009JB006882.

Li, X., Kind, R., Yuan, X., Wölbern, I., and Hanka,W., 2004. Rejuvenation of the lithosphere by the Hawaiian plume. Nature 427, 827–829.

Li, X., Yuan, X., and Kind, R., 2007. The lithosphere-asthenosphere boundary beneath the western United States. Geophys. J. Int. 170, 700-710.

Nábelek, J., Hetényi, G., Vergne, J., et al., 2009. Underplating in the Himalaya-Tibet collision zone revealed by the Hi-CLIMB experiment. Science 325, 1371-1374.

Rychert, C. A., Rondenay, S., and Fischer, K. M., 2007. P-to-S and S-to-P imaging of a sharp lithosphere-asthenosphere boundary beneath eastern North America. J. Geophys. Res. 112, B08314, doi:10.1029/2006JB004619.

Rychert, C.A., Shearer, P.M., 2009. A global view of the lithosphere-asthenosphere boundary. Science 324, 495–498.

Savage, B., and Silver, P.G., 2008. Evidence for a compositional boundary within the lithospheric mantle beneath the Kalahari craton from S receiver functions. Earth Planet. Sci. Lett. 272, 600–609.

Wei, Z.G., Chen, L., Xu, W.W., 2011. Crustal thickness and Vp/Vs ratio of the central and western North China Craton and its tectonic implications. Geophys. J. Int. 186, 385-389.

Wen, L., Helmberger, D. V., 1998. A two-dimensional P-SV hybrid method and its

application to modeling localized structures near the core-mantle boundary. J. Geophys. Res. 103, 17,901-17,918.

Wittlinger, G., and Farra, V., 2007. Converted waves reveal a thick and layered tectosphere beneath the Kalahari super-craton. Earth Planet. Sci. Lett. 254, 404-415.

Zhao, L., Allen, R.M., Zheng, T., Zhu, R., 2012. High-resolution body wave tomography models of the upper mantle beneath eastern China and the adjacent areas. Geochem. Geophys. Geosyst. 13, Q06007, doi:10.1029/2012GC004119.

Zhu, L. & Kanamori, H., 2000. Moho depth variation in southern California from teleseismic receiver functions. J. geophys. Res. 105, 2969–2980.

Zhu, R.X., Zheng, T., 2009. Destruction geodynamics and Paleoproterozoic plate tectonics of the North China Craton. Chinese Science Bulletin 54 (19), 3354–3366.

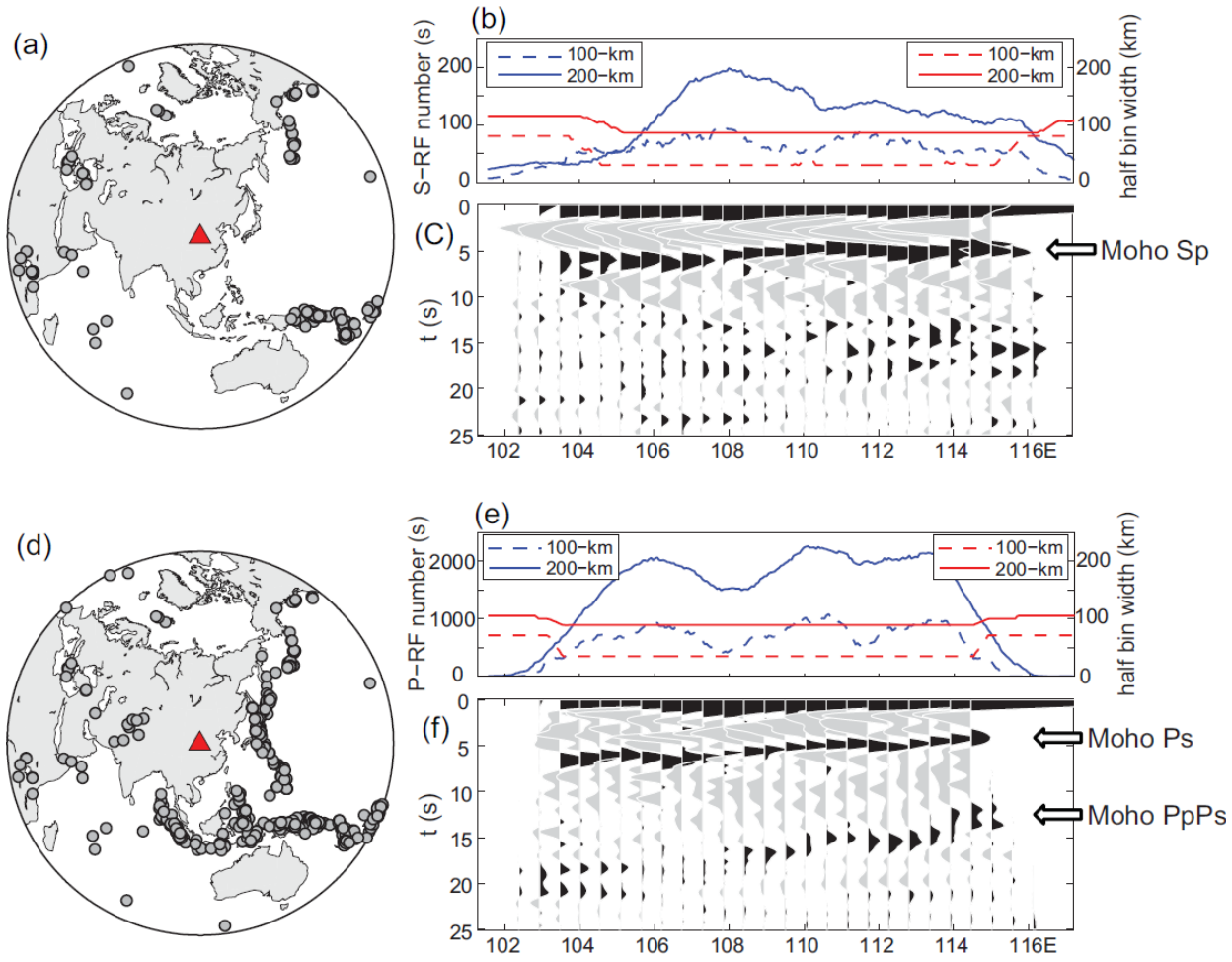

Figure DR1. Distribution of teleseismic events used (a, d), numbers of RFs in the bins (blue traces) and bin widths (red traces) used in the CCP stacking at 100 and 200 km depths (b, e) and stacked RF sections (c, f) with frequencies 0.03 – 0.5 Hz after moveout corrected to p = 0. (a, b, c) for S RFs and (d, e, f) for P RFs. The Moho conversion phases (Sp in S RFs and Ps in P RFs) and strong multiple (PpPs in P RFs) are marked by arrows in (c, f).

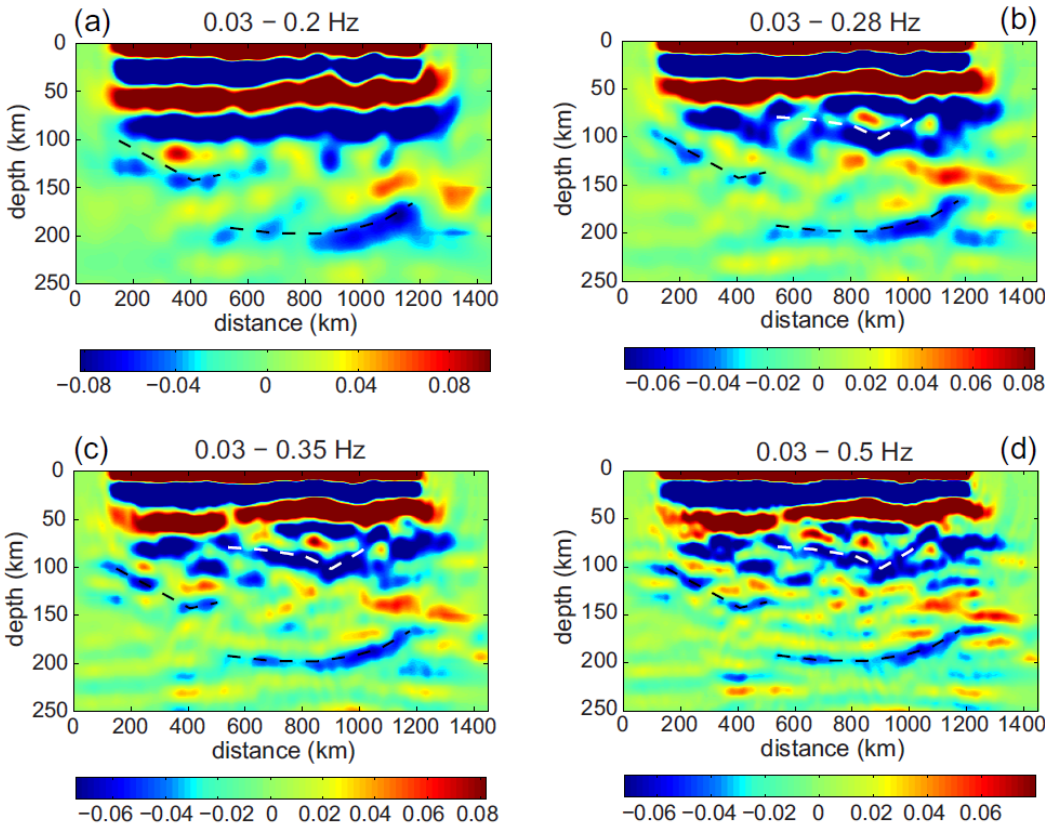

Figure DR2. Migrated S RF images for profile A-A' obtained by using different frequency contributions of the data: (a) 0.03 – 0.2 Hz; (b) 0.03 – 0.28 Hz; (c) 0.03-0.35 Hz; (d) 0.03 – 0.5 Hz. The ILD and the LAB are marked as white and black dashed lines, respectively.

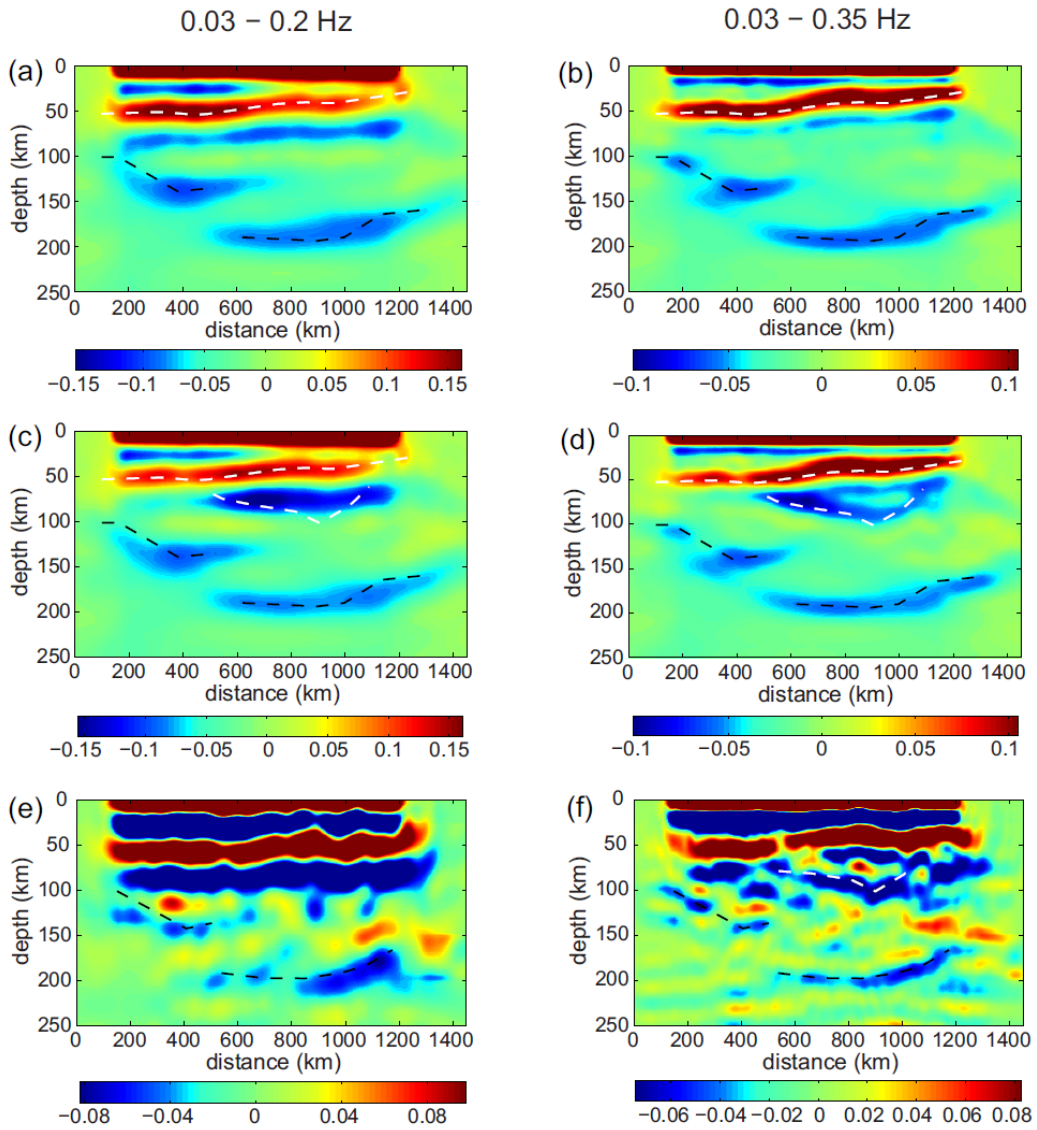

Figure DR3. Migrated S RF images of different frequency contents for two synthetic models (a-d) and from the real data for profile A-A' (e, f). (a, c, e) 0.03 – 0.2 Hz; (b, d, f) 0.03 – 0.35 Hz. The synthetic models contain a Moho and a LAB, with (c, d) or without (a, b) an ILD built in. All the discontinuities in the synthetic models were designed to resemble the imaged real structure, and the synthetic images were constructed based on the actual data coverage. Both the modeled and observed LABs are marked as black dashed lines. The modeled Moho and ILD and the observed ILD are marked as white dashed lines. Although the amplitudes show some changes, the overall feature of the synthetic images, especially that of the LAB is essentially the same no matter an ILD was built into the model or not. The deformed and/or intermittent LAB image in the left part of both the synthetic and data images might be a result of limited data coverage (Fig. DR1b).

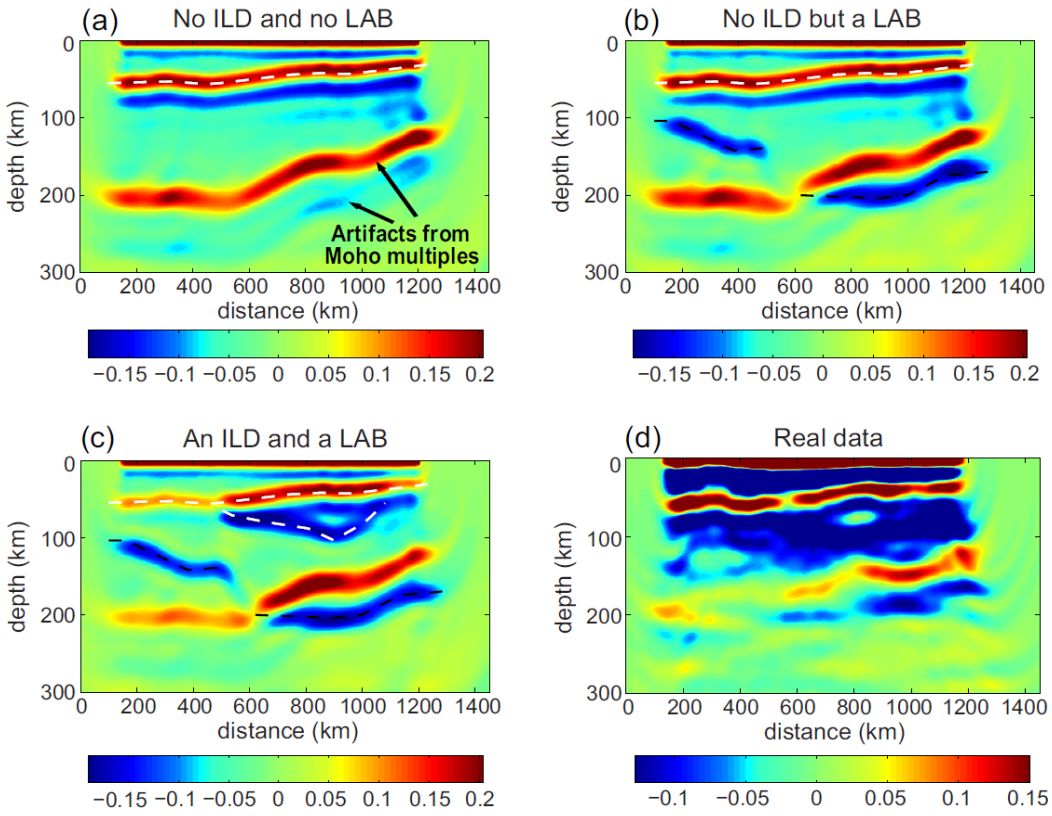

Figure DR4. Migrated P RF images with frequencies 0.03 – 0.35 Hz for three synthetic models (a-c) and from the real data for profile A-A' (d). The synthetic models contain no ILD and no LAB (a), no ILD but a LAB (b), or both an ILD and a LAB (c), respectively. The synthetic models in (b) and (c) are the same as those used in Figs. DR3a-DR3b and DR3c-DR3d, respectively. The Moho and the ILD in the synthetic models are marked as white dashed lines and the LAB as black dashed lines. Artifacts induced by the positive PpPs and negative PsPs + PpSs multiples of the Moho are marked in (a). Without a LAB built in the synthetic model (a), the negative multiples of the Moho are much weaker and parallel to slightly steeper than the positive multiple of the Moho. In the data image (d), the negative signal at 150-200 km depths appears equally or even stronger and has a smaller dipping angle, especially in the middle part of the profile, than the above positive Moho multiple artifact. These image features bear considerable resemblance to the synthetic images with a LAB at the similar depths (b, c). The presence of an ILD has no significant effects on the image feature of the modeled LAB, although it affects the amplitudes of the LAB Ps phase and other signals, especially in the left part of the image (compare b and c).

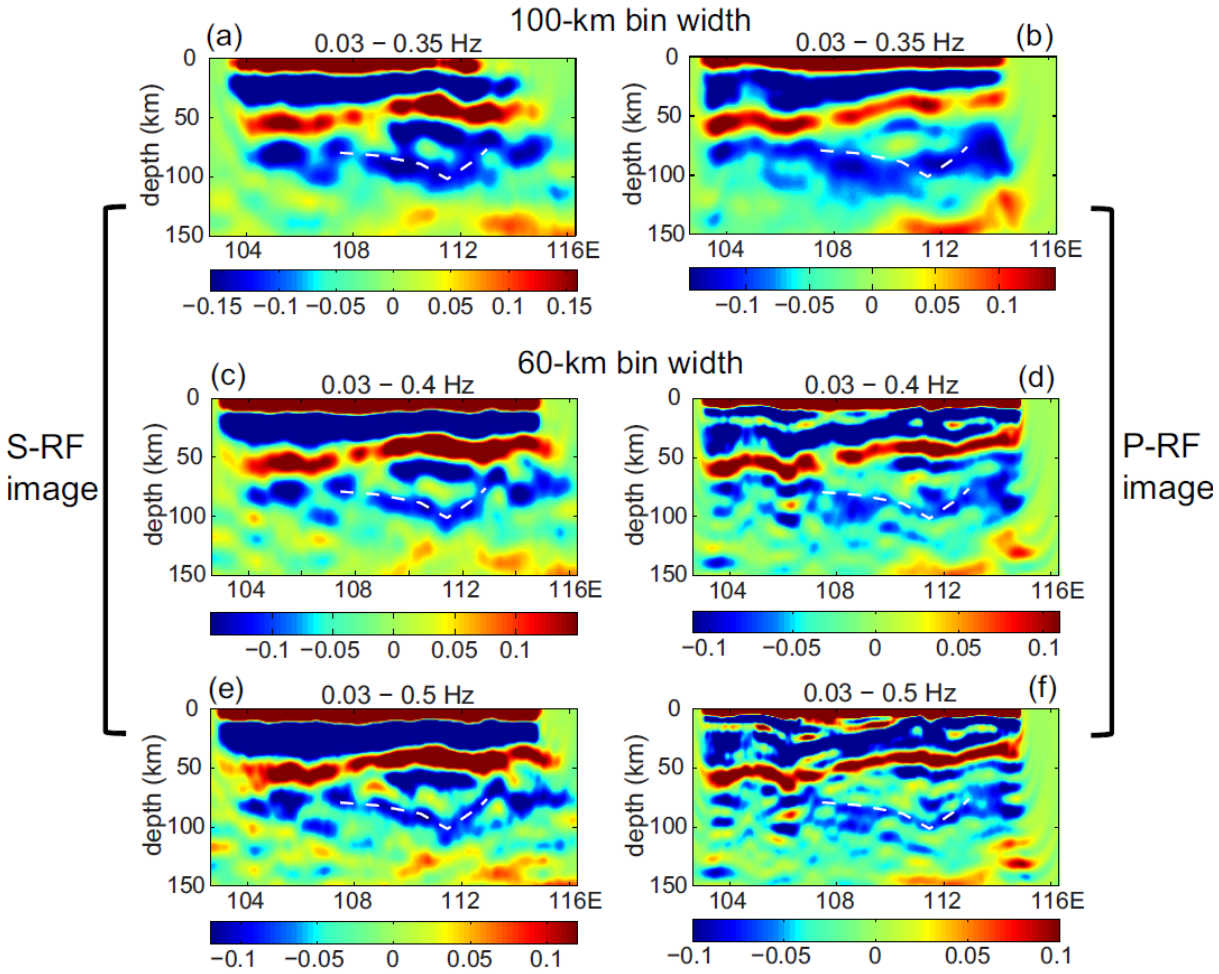

Figure DR5. Migrated S RF images (a, c, e) and P RF images (b, d, f) for profile A-A'. Different frequency contributions of the data and stacking bin widths (lateral smoothing) were considered in RF imaging: (a, b) 0.03 – 0.35 Hz with 100-km bin width at 100 km depth; (c, d) 0.03 – 0.4 Hz and (e, f) 0.03 – 0.5 Hz with 60-km bin width at 100 km depth. White dashed Line in each panel marks the ILD identified in the RF images. (e, f) are same as Fig. 2C and 2D.

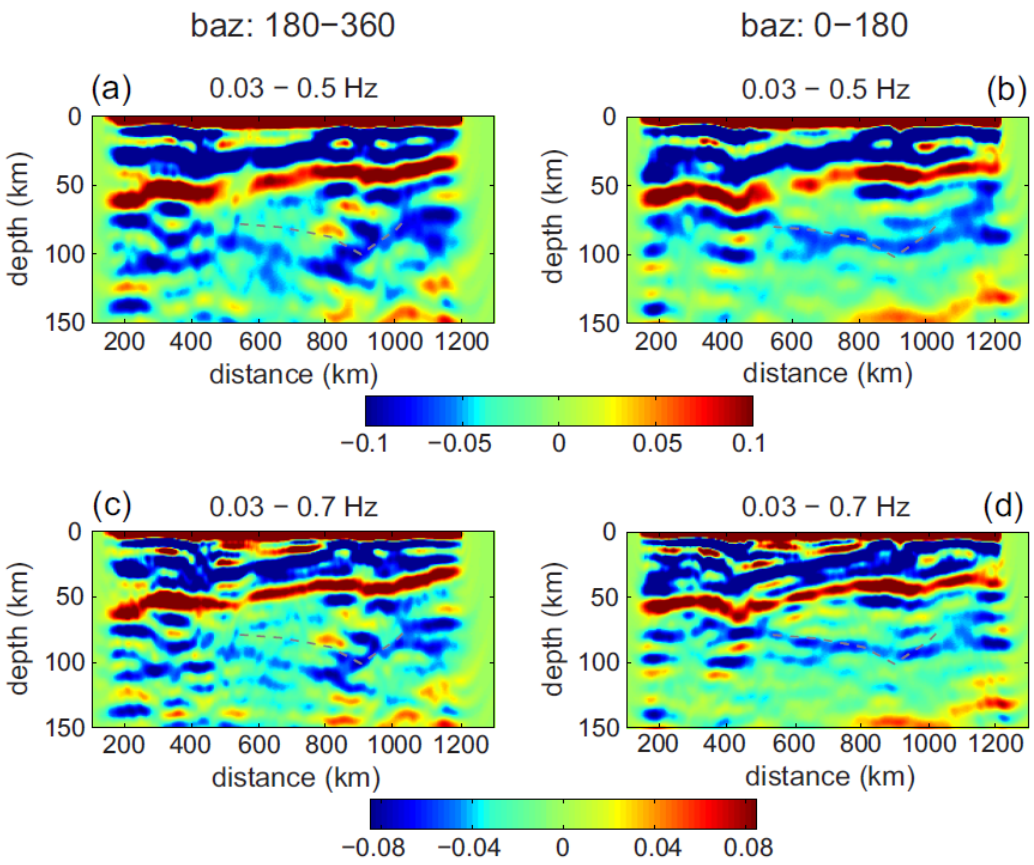

Figure DR6. Migrated P RF images from two subsets of the real data in non-overlapping back azimuth ranges: 180º– 360º (a, c) and 0 – 180º (b, d). All the 3061 P RFs in the first subset and randomly selected 3061 out of 7639 P RFs in the second subset were used to construct the images. Different frequency contributions of the data were considered in imaging: (a, b) 0.03 – 0.5 Hz; (c, d) 0.03 – 0.7 Hz. Gray dashed lines are same as the white dashed lines in Fig. DR5. Comparisons of the images provide further constraints on the nature of the two negative signals observed at ~80 -120 km depths in Fig. 2D, Figs. DR5f and DR5d. For seismic rays coming from east (back azimuths within 0º - 180º), the eastward dipping part of the shallower signal is clearly identified, but the similarly eastward dipping signal below it appear much weaker, even invisible in the image (b, d). Using the subset of data from west (180º - 360º), on the other hand, the former weakens, while the latter becomes more predominant (a, c). The image strength of the westward dipping part of the shallow signal changes with incident direction of P waves in a similar way to its eastward dipping counterpart. Moreover, this westward dipping part was imaged at different locations using the two subsets of data, being more to the east with the data coming from east (compare b, d with a, c). All these image features of the shallow signal are consistent with the theoretical predictions for Ps phases and the previous synthetic and data images for dipping discontinuities (Chen et al., 2005; 2006). The image of the

deeper signal appears to be affected by the coming direction of data in an opposite way, resembling the artifacts induced by crustal multiples but bearing large differences from the modeled Ps images (Chen et al., 2006). Using all the P RFs or other groups of randomly selected 3061 P RFs in the second subset results in very similar images to those shown in (b, d). These image comparisons combined with the consistent depths in the S and P RF images (e.g., Figs. 2C and 2D) suggest that the shallower negative signal likely represents a real structure in the upper mantle, whereas the deeper signal may be an artifact induced by crustal multiples.

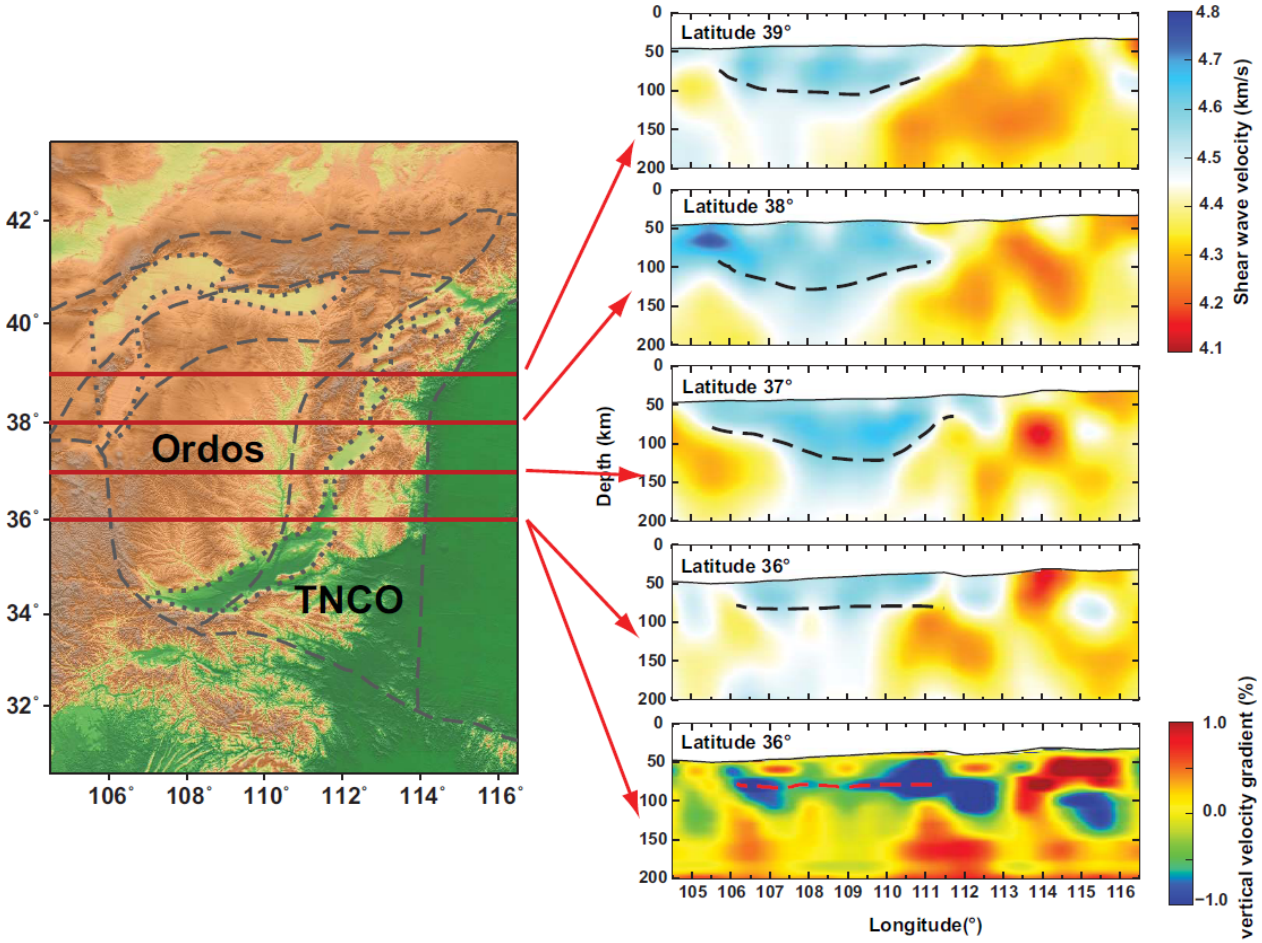

Figure DR7. Shear-wave velocities along four E-W profiles crossing the TNCO and the Ordos block (latitudes 36°N, 37°N, 38°N, 39°N) and vertical velocity gradients along the 36°N profile obtained by 3-D regional surface wave tomography (Jiang et al., 2013). A relatively low-velocity layer was observed at 80-150 km depth within the high-velocity mantle root along all the profiles, with the depths of the maximum velocity reductions marked by the dashed curves.